J Mater Sci (2012) 47:1758–1766
DOI 10.1007/s10853-011-5956-z

Microstructure dependence of the magnetic properties of sintered Ni–Zn ferrites by solid-state reaction doped with V_2O_3

G. Herrera · M. M. Pérez-Moreno

Received: 12 August 2011 / Accepted: 13 September 2011 / Published online: 27 September 2011

Abstract In order to improve the frequency range operation of Ni–Zn ferrites with the $Ni_{0.7}Zn_{0.3}Fe_2O_4$ stoichiometry in this study, they were doped with V_2O_3 at different concentrations (0, 0.25, 0.50, and 0.75 wt%). The samples were prepared by the solid-state reaction at 1250 °C for 24 h. The content and location of Vanadium in these ferrites allow us to determine its influence on their microstructure and magnetic properties. A single cubic spinel phase with lattice parameter variation was determined by the refinement of X-ray diffraction patterns. This refinement was achieved using the Rietveld method. The lattice parameter presents a slight enhancement with increasing Vanadium content up to 0.50 wt% of V_2O_3. The increase of intragrain porosity and the segregation of Vanadium at the grain boundary in samples with higher concentration of Vanadium show a narrow grain-size distribution that leads to a resonant character of the magnetic domain wall. A wide grain-size distribution determined in lower concentration of Vanadium results in a mixed resonant-relaxation dispersion. The use of V_2O_3 as a dopant in Ni–Zn ferrites increases the frequency operation and coercivity, H_c, without abruptly degrading the saturation magnetization, M_s. We, therefore conclude, that Vanadium may be used as a strong dopant for the preparation of ferrites for any particular high-frequency application.

G. Herrera · M. M. Pérez-Moreno
Departamento de Química Inorgánica, Facultad de Ciencias Químicas, Universidad de Valencia, Burjasot, 46100 Valencia, Spain

G. Herrera (✉)
Department of Inorganic Chemistry, University of Valencia, Calle Doctor Moliner, 50, Burjasot, 46100 Valencia, Spain
e-mail: guillermo.m.herrera@uv.es

Introduction

Ferrites are considered as soft magnetic materials. The most important types of ferrites are manganese–zinc (Mn–Zn) and nickel–zinc (Ni–Zn) ferrites [1]. Mn–Zn ferrites have a high permeability, and so they are used as inductor cores, but they are limited to low-frequency operation. Ni–Zn ferrites have been intensely studied because of their remarkable high-frequency operation (1–100 GHz) as well as because they exhibit high chemical stability and high permeability in the radiofrequency region [2] Ni–Zn ferrites are used in telecommunications as high-frequency inductive components, such as transformer cores, rod antennas, radiofrequency coils, multilayer chip inductors [3], wave absorbers, and converters. Recently, they were used as radar-absorbing materials. At low frequencies, this interaction is small, and the eddy current losses are negligible. However, at high frequencies, the interaction causes unique phenomena, leading to application in microwave ferrite devices [4], such as telecommunication in cellular telephones and reception/transmission antennas [5], frequency-tuneable oscillators and filters, isolators, circulators, and phase shifters [6]. Other specialized application of Ni–Zn ferrites is in the magnetic cores of read/write heads for high-speed digital tape or disk recording [7]. Many literatures are available on these aspects of the $Ni_{1-x}Zn_xFe_2O_4$ ferrites with relatively higher Zn content (x in the range 0.4–0.7) [8, 9]. However, the related literatures on low Zn-bearing ($x \leq 0.3$) ferrites are very rare. That is the reason, the present composition $Ni_{0.7}Zn_{0.3}Fe_2O_4$ has been selected for the investigation. It is known that the best

value of radiation attenuation was reported to be about 70% in Ni–Zn ferrite by Lima et al. [5].

$NiZnFe_2O_4$ follows the spinel structure Fd$\underline{3}m$ (Oh^7) No. 227 [1] with formula, $[Fe^{3+}_{1-x}Zn^{2+}_x]^{tet}$ $[Ni^{2+}_{1-x}Fe^{3+}_{1+x}]^{oct}$ O_4. $[Fe^{3+}_{1-x}Zn^{2+}_x]^{tet}$, and this means that the $[Fe^{3+}_{1-x}Zn^{2+}_x]$ ions occupy the tetrahedral, Td (A) sites, whereas $[Ni^{2+}_{1-x}Fe^{3+}_{1+x}]$ ions occupy the octahedral, Oh (B) sites of the lattice structure [10, 11]. Wyckoff positions for (A) site, (B) site, and O_{2-} are 8a, 16d, and 32e, respectively. Therefore, in the unit cell structure, Fe^{2+} (0.75 Å) may replace Zn^{2+} (0.74 Å), while V^{3+} (0.78 Å) can exchange sites with Fe^{3+} (0.64 Å). This cation exchange depends on the sintering conditions, since the Oxygen partial pressure affects Vanadium and Iron oxidation states and, hence, influences the magnetic properties of the ferrite.

The typical synthesis method to achieve the total reaction of reagents to obtain the Ni–Zn ferrite is the solid-state reaction. Usually, in this ceramic technique, the raw materials are mixed in stoichiometric proportions in a ball mill for a sufficient period of time. The duration of milling will determine the grain-size distribution, which in turn will influence the homogeneity of the compact that goes into the final firing as well as the microstructure after the sintering process. The optimum grain size is generally of the order of 1 μm. The mixed powders are pre-heated at an intermediate temperature (800–900 °C). The purpose of pre-heating is to propitiate the process of forming the ferrite lattice. The obtained ferrite, the powders, can be mixed with a binder with an appropriate ratio and then subjected to pressure for compacting. Then, the compacted ferrites can be sintered in a range of temperatures between 1200–1400 °C to complete the inter-diffusion of the component metal ions into the preferred crystal lattice. It is well known that the dominant microstructural parameters which are important for achieving high permeability are a high-sintered density, a large average grain size, and a stress-free grain boundary. In order to promote grain growth and densification, an appropriate liquid phase can be applied. However, the presence of a liquid phase during sintering can induce the transition from normal to anomalous grain growth and induce chemical and physical changes on the grain boundaries, which may degrade the magnetic permeability [12]. In particular, it has been shown that small amounts of Vanadium pentoxide (V_2O_5) tend to remain at the grain boundary region, acting as liquid phase sintering aids [13]. The impact of another Vanadium compound, namely, Vanadium trioxide (V_2O_3 with a melting point of 1790 °C) remains to be established in these ferrite systems.

The main objectives of the present study are the following. First, to prepare Ni–Zn ferrites to improve their applications at the high-frequency range without abruptly degrading their magnetic properties such as: their Curie temperature, T_C, coercivity, H_c, initial permeability, μ_i, and saturation magnetization, M_s. Therefore, a series of ferrites with $Ni_{0.7}Zn_{0.3}Fe_2O_4$ stoichiometry with increasing contents of V_2O_3 (used as dopant) have been prepared by the solid-state reaction. The chemical distribution, and the location and content of Vanadium in these ferrites will allow for the determination of its influence on the structure, microstructure and magnetic properties of the ferrites mentioned above.

Experimental procedure

Materials

Polycrystalline Ni–Zn ferrites with $Ni_{0.70}Zn_{0.30}Fe_2O_4$ stoichiometry were prepared by the solid-state reaction. Weighed amounts of the raw oxide NiO (Sigma-Aldrich, 99%), ZnO (Cerac, 99.5%) and Fe_2O_3 (Cerac, 99.95%) were mixed with ethanol (Sigma Aldrich, 70% in H_2O) to form a homogeneous slurry. This was milled in an attritor mill (Union Process 01HD) system for 8 h. The grinding media to material charge ratio was 1:3 using 1/8 inch diameter stainless steel balls. The steel balls were cleaned and weighed after the milling to recover the material impregnated on the steel ball. The milled powders were heated at 900 °C during 5 h in air in a programmable Thermolyne 47900 muffle furnace. After that the powders were doped with different concentrations of V_2O_3 (Sigma-Aldrich, 99.99%) 0.0, 0.25, 0.50 and 0.75 wt% in an aqueous environment. At this stage, doped powders were milled during 2 h in an agate mortar. The dry powder was plasticized with 10 wt% of a PVA polyvinyl alcohol) aqueous solution used as a binder. The resulting material was dried and formed into a toroidal shape (outer diameter 20 mm, inner diameter 12 mm height about 3.5 mm) exerting an uniaxial pressure of 3 ± 0.5 MPa for 1 min. in a Carver CMG-30-15 press. The first step in the heat treatment for the compacted specimens is the removal of the binder at 800 °C. Then the samples were sintered at 1250 °C during 24 h. After sintering the samples were stabilized in a 0.2% O_2/N_2 atmosphere and were then cooled under equilibrium conditions. To control Fe^{2+} ions an inert gas such as N_2 is needed. Oxygen gas is needed to avoid dissociation of ZnO and hence Zn loss which might occur by Zn vaporization [14]. The heating and cooling temperature ramps had a slope of 10 °C/min. The heat treatment was performed in a programmable Carbolite (model STF 15/-/450) tubular furnace equipped with Eurotherm 2416CG control.

Characterization techniques

The crystalline phases were identified using a Bruker X-ray powder diffactometer—AXS B8—Advance using λ(Cu

K_α) = 1.54 Å. The X-ray diffraction (XRD) patterns of Ni–Zn ferrites were collected at room temperature with a step size of 0.02 $2\theta°$ and a counting time of 10 s. The determination of the lattice constant and other structural parameters of the spinel phase were made from the X-ray diffraction patterns using the Rietveld method. The refinement was performed with Fullprof98 [15], available in the software package Winplotr [16]. The refinement involved the following parameters: scale factor; zero displacement correction; unit cell parameters; peak profile parameters using a pseudo-Voight function and overall temperature factor. The structural parameters and atomic positions for the spinel phase were taken from the literature.

The density was evaluated by the Archimedes's method in an analytical balance Mettler Todelo model AB104. The density value was determined by the relation $\rho = \frac{A*(\rho_0-\rho)}{A-B} + \rho_L$ where A is the weight of the sample in air, B is the weight of the sample under liquid, ρ_0 is the density of the liquid, and ρ_L is the air density. The measurements were taken at 20 °C, where $\rho_0 = 0.99823$ g/cm^3. The surface of the sintered samples were polished in a cloth rotating wheel using fine alumina particles with an average size of 0.5 μm size. The samples were etched in a mixture of 20 mL HNO_3, 5 mL HF and 40 mL H_2O for 1 min. Then the samples were heated during 2 h in a muffle furnace. The fractured surfaces were analyzed by scanning electron microscopy (SEM) using a steroscan 440 Leica Cambridge electron microscope. The micrographs were taken with magnifications between 2.5 k× and 3.0 k× with a voltage of 20 kV, a current intensity of 1000 pA and a work distance of 25 mm. Energy dispersive X-ray (EDX) microanalysis or point composition were established in the grain and grain boundaries. These studies and analysis were performed on the same equipment, with an Oxford/Link System electron probe microanalyzer (EPMA). For Curie temperature, T_C, determination, sintered samples were coiled as a transformer and placed in a muffle furnace according to the experimental setup described in the literature [17].

The high-frequency measurements (Cole–Cole representations) were carried out at room temperature using a network analyzer Agilent model 8753ES. This equipment allows measurements, in a wide range of frequency (from 30 kHz to 6 GHz), at a constant current of 300 μA. The whole system is controlled by a PC computer with measurement software developed in our laboratory. This software allows a frequency run of ~400 points in less than 2 min. For this evaluation we used toroidal samples (outer diameter 20 mm, inner diameter 12 mm, and height about 3.5 mm) wound as transformers with 17 turns of 30 AWG cooper wire.

The magnetic characterization was performed using cylindrical samples with a vibrating sample magnetometer (VSM EG & G Princeton Applied Research Corporation model LDJ 9600) at 300 K, with a maximum external magnetic field 5000 Oe.

Results and discussion

Effects of V_2O_3 doping on the spinel structure

The XRD patterns confirm the single phase cubic spinel structure. The identification of crystal phase was made with the powder diffraction File No. 10-0325; see Panel (a) of Fig. 1. The refinement was continuous until convergence was reached with a goodness factor very close to 1. The observations we collected from our XRD patterns are consistent with those reported earlier [18, 19]. The values

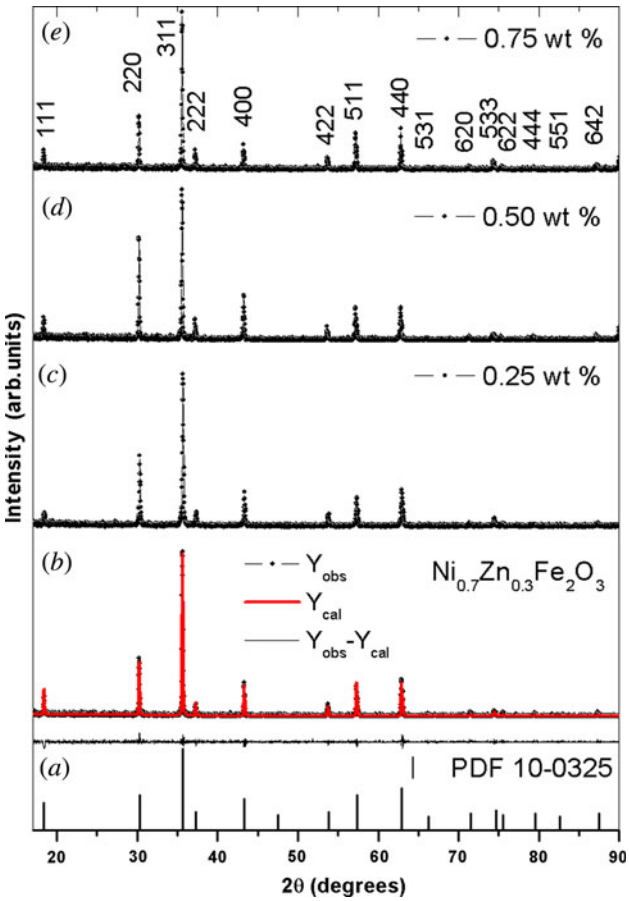

Fig. 1 XRD results for $Ni_{0.7}Z_{0.3}Fe_2O_4$ ferrites: (*a*) Peak positions of powder diffraction File No. 10-0325. (*b*) Rietveld refined X-ray diffraction pattern of $Ni_{0.7}Z_{0.3}Fe_2O_4$ ferrites, figure shows the observed intensity (Yobs), the calculated intensity (Ycalc) and the difference between observed and calculated intensities (Yobs–Ycalc). (*c*) XRD for sample with 0.25 wt% of V_2O_3. (*d*) XRD for sample with 0.50 wt% of V_2O_3. (*e*) XRD for sample with 0.75 wt% of V_2O_3

Table 1 Crystallographic data and results of Rietveld refinement of X-ray diffraction patterns of $Ni_{0.70}Zn_{0.30}Fe_2O_4$ ferrites sintered at 1250 °C for 24 h, in which spinel is detected as single crystalline phase

V_2O_3 (wt%)	0	0.25	0.50	0.75
a (Å)	8.3506 (8)	8.3556 (2)	8.3587 (5)	8.3584 (5)
V (Å^3)	582.31 (3)	583.35 (4)	584.00 (4)	583.94 (1)
R_p (%)	9.27	8.98	9.66	9.34
R_{wp} (%)	10.5	10.3	10.4	10.6
R_{wp} (expected) (%)	10.02	9.61	9.72	10.05
χ^2	1.07	1.05	1.10	1.08

of the reliability factor of refinement (R_{wp}); quality of fit index (χ^2) and the refined lattice parameter of Ni–Zn ferrites for all specimens heated at 1250 °C for 24 h are shown in Table 1. The lattice parameter enhances slightly with increasing Vanadium content up to 0.50 wt% of V_2O_3. The expansion of the unit cell as the Vanadium content increases in the Ni–Zn ferrites is in agreement with the idea of expansion of the lattice cell as a small ion Fe^{3+} is replaced by a larger one V^{3+}. Figure 1b–e shows the evolution of XRD patterns and the refinement of the XRD powder pattern for undoped Ni–Zn ferrite. Other possibility of the lattice expansion which may be attributed to the reduction of Fe^{3+} and formation of Fe^{2+} ions of larger ionic radius, which probably dissolve in the spinel lattice. At temperatures higher than 1200 °C, loss of zinc due to volatilization takes place, which, for charge compensation reasons, results in the formation of Fe^{2+} ions.

Effects of V_2O_3 doping on the densification mechanism

In Table 2 one can observe the drop of sintered density as the dopant concentration is increased. The theoretical density value was 5.305 g/cm^3. In previous studies drop of density value of the ferrite doped with V was observed [20–23]. In particular, Hsu et al. [21] and Hu et al. [23] refer to the drop of density as due to the formation of the Vanadium-rich phase. Jean and Lee suggest that the density drop is due to the fact that, a poor distribution of a small amount of V causes non uniform shrinkage firing [22]. Hossain et al. [10] suggest the use of high temperatures to cause a decrease in density, because, in this case, the intragrain porosity increases. This argument is in agreement with our SEM results discussed in the next section.

Table 2 Green and sintered density[a], the % of theoretical density (*TD*) and grain size[a] of sintered $Ni_{0.70}Zn_{0.30}Fe_2O_4$ ferrites with different vanadium content

V_2O_3 concentration (wt%)	Green density (g/cm^3)	Sintered density (g/cm^3)	TD (%)	Grain size (μm)
0	2.85 (8)	5.12 (5)	96.51 (2)	4.81 (4)
0.25	2.85 (8)	5.10 (4)	96.13 (5)	4.28 (4)
0.50	2.92 (1)	4.96 (3)	93.49 (3)	5.00 (5)
0.75	2.92 (9)	5.01 (4)	94.43 (9)	6.45 (5)

[a] Averaged at least over five measurements

Effects of V_2O_3 doping on microstructure

Figure 2a and b shows the SEM micrographs used to analyze the microstructure over the fracture surfaces. The presence of intragrain and intergrain porosity with non-homogeneous grain shape distribution (Table 2) can be clearly seen. The seemingly big grains may be attributed to vanadium, which accelerates the grain growth rate [24].

Both micrographs show clear differences on the fracture surface respect to the micrograph related to ferrite without V_2O_3 [25]. The intragrain porosity propagation is due to the tendency of Zn to evaporate from the spinel structure under high temperature. The possible reasons to explain the presence of intergrain porosity are: (i) the use of an Oxygen-rich atmosphere [12], (ii) the influence of dopants such as V seem to segregate on the grain boundary [26], (iii) the melting of V forms a liquid phase at grain boundaries increasing the number of pores that are trapped within the grains, iv) the V evaporation due to the prolonged heat treatment leaving the ferrite grain boundaries without a large excess of a V-rich phase; [27], and (vi) the cation vacancy flux generated by V addition increases the pore mobility toward the grain boundaries [14, 28, 29]. All these factors contribute to the reduction of the sintered density as one can observe in Table 2. Sun et al. reported that R_2O_3, for some R = transition metal or rare-earth ions cannot continue to enter into the lattice, but form secondary phases such as $RFeO_3$. This destroys the homogeneous composition and microstructure [30]. On the other hand, micrographs labels (c–f) taken at the polished and etched surface of the toroid, shows the homogeneity of the grain shape distribution at the surface. This result is in agreement with Schichijo et al. [31] In this study the authors suggest that the effect of the increased V_2O_3 concentration is to produce a homogeneous shape microstructure with relative small grain size. Narayan et al. [27] refer that the rounding of the grains and their shape are because the grains are separated by the liquid phase. Also when we increase the V_2O_3 wt%, the grain-size distribution analysis reveals a bimodal behavior as reported by Lebourgeois et al. [32]. It is known that V_2O_3 is not a stable phase, and the use of an Oxygen atmosphere, during high heat treatments of Vanadium (V^{3+}) ions, could cause oxidation of the Vanadium (V^{5+}) ions. This assumption leads to the presence of a liquid phase [27] during sintering. A consequence of this is the

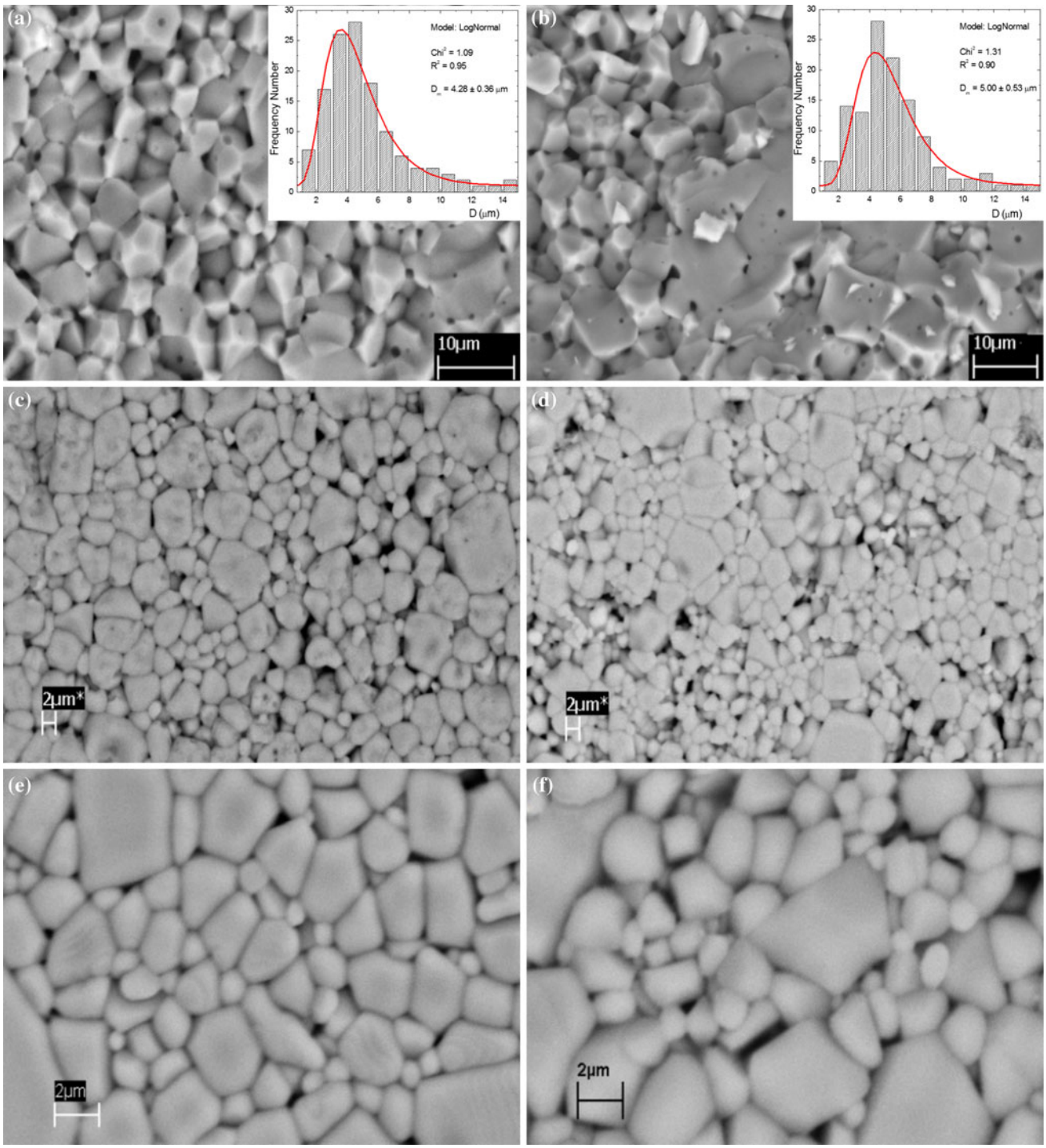

Fig. 2 SEM micrographs taken on fracture of $Ni_{0.7}Z_{0.3}Fe_2O_4$ samples sintered at 1250 °C during 24 h. (**a**) 0.25 wt%, (**b**) 0.50 wt%. Evolution of SEM micrographs taken on the polished surface of toroids, (**c**) V_2O_3 0 wt%, (**d**) 0.25 wt%, (**e**) 0.50 wt%, (**f**) 0.75 wt%

transition from normal to anomalous grain growth [13, 21, 23]. According to the arguments presented in the effects of V_2O_3 doping on the densification mechanism section, this result leads to the precipitation of a V-rich phase at the grain boundaries [33] as can be observed in the EDX results. The mean grain size (Table 2) was determined by means of Image J software [34] over an average of five SEM micrographs. In the insets (Fig. 2a, b), histograms fitted with a Log-normal curve can be seen as Jankovskis reported in a previous study [35].

Figure 3a and b shows the chemical composition determined by EDX along the grain and grain boundaries

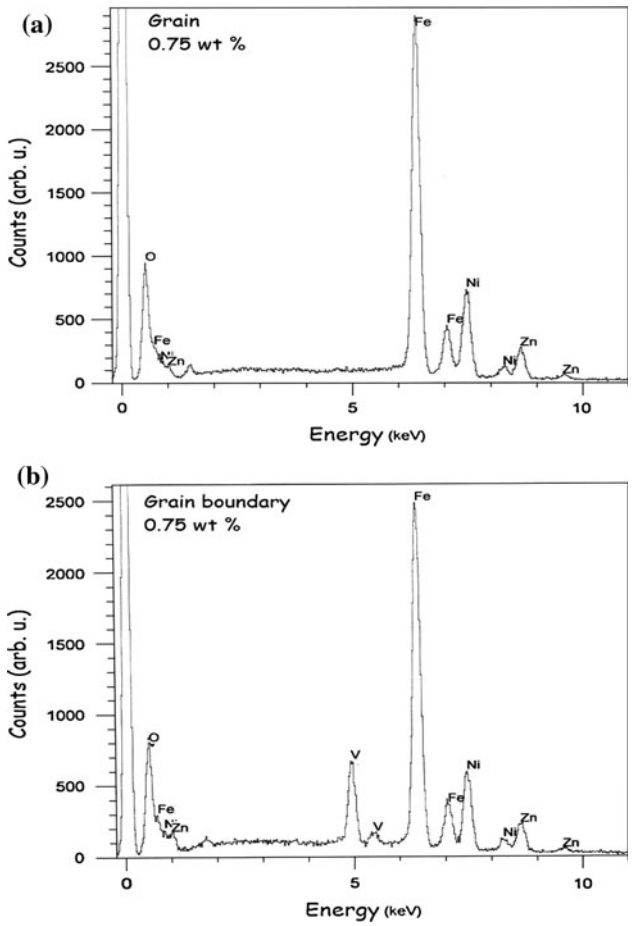

Fig. 3 EDX spot analysis, in which the electron beam was stopped and positioned on: (**a**) the center of the grain, and (**b**) the grain boundary in a 0.75 wt%-V_2O_3 doped sample

for the sample doped with 0.75 wt% of V_2O_3. The elemental concentration results for the sample without dopant are in agreement with a previous study [36] (therein, the mean of five values were taken at the center of the grain and at the grain border). Tables 3 and 4 show the chemical composition for global and point-to-point EDX analysis on the grain boundary. One can observe the formation of a V-rich phase situated at the grain boundary. This result is in agreement with those previously reported in the literature, [14, 21, 37]. However, the presence of a second phase related to V was not detected by XRD measurements.

Effects of V_2O_3 doping on magnetic properties

Curie temperature

The permeability thermal spectra of the samples were used as a test of the formation and the homogeneity of the samples as well as an indication on the growth and the quality of the grains. The μ_i–T (Fig. 4) profile showed a

Table 3 SEM/EDX global composition microanalysis results (wt%)[a] for samples $Ni_{0.70}Zn_{0.30}Fe_2O_4$ ferrites with different vanadium contents

V_2O_3 concentration	Niquel	Zinc	Iron	Vanadium
0.0	18.94 (5)	6.43 (2)	52.31 (4)	0.0
0.25	19.54 (4)	6.46 (5)	52.65 (5)	0.76 (2)
0.50	18.30 (5)	5.75 (3)	53.24 (5)	1.20 (5)
0.75	19.16 (5)	6.33 (5)	53.11 (4)	1.12 (5)

[a] Averaged at least over five analysis

Table 4 SEM/EDX point-to-point composition microanalysis results (wt%)[a] for samples $Ni_{0.70}Zn_{0.30}Fe_2O_4$ ferrites with different vanadium contents

V_2O_3 concentration	Niquel	Zinc	Iron	Vanadium
0.0	16.84 (4)	7.83 (3)	44.13 (3)	0
0.25	16.76 (3)	8.68 (3)	43.22 (3)	0.84 (2)
0.50	16.80 (5)	9.03 (3)	42.64 (3)	1.09 (4)
0.75	16.33 (5)	7.28 (4)	45.27 (4)	6.90 (5)

[a] Averaged at least over five analysis

sharp peak followed by a "vertical" decrease of the permeability that determines accurately the Curie temperature, T_C. For each composition, almost constant values of T_C were obtained. The vertical drop indicates that the samples show both homogeneous ionic structure and homogeneous grain-size distribution [17]. On the other hand, the permeability amplitude (as a good source of information on the grain growth) decreases with an increase in the V_2O_3 concentration. This result means that samples without dopant and with 0.25 wt% of V_2O_3 show a wide grain-size distribution, and thus, the μ–T curve was more peaked. The samples with 0.50 and 0.75 wt% of V_2O_3 were more sensitive to grain-boundary effects, and thus, the μ–T curve was less peaked. The profile also shows a Hopkinson's peak near the T_C, a behavior normally exhibited by cubic structures like those of the samples analyzed in this study [38]. Table 5 shows the compositional dependence of T_C.

Complex permeability

The decrease of μ_i and increase of frequency (Table 5) were reported using complex impedance technique [39–42]. This behavior is in accordance with Snoek's law [43]. The decrease in the permeability can be explained by the microstructural changes. The intergrain porosity around the grains introduces wall discontinuities across the grain boundaries. Also, the intragrain porosity and the presence of Vanadium at the grain boundary are supposed to pin the domain walls, resulting in a decrease of the permeability and an increase of the magnetocrystalline anisotropy [30].

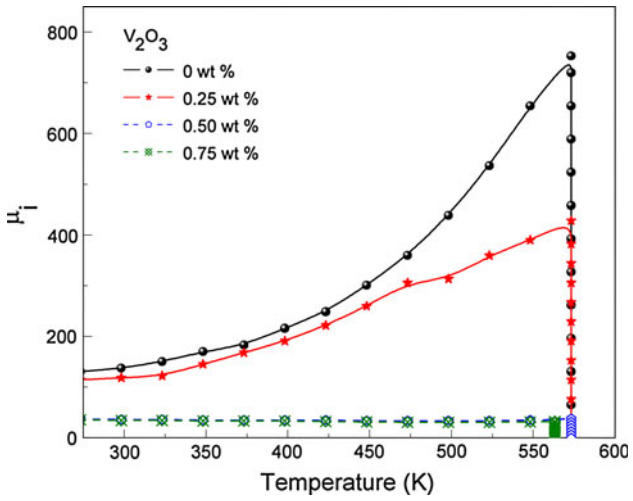

Fig. 4 Comparison between the permeability thermal spectra for $Ni_{0.7}Z_{0.3}Fe_2O_4$ ferrites with 0, 0.25 wt% (*solid line*); 0.50 and 0.75 wt% of V_2O_3 (*dash line*)

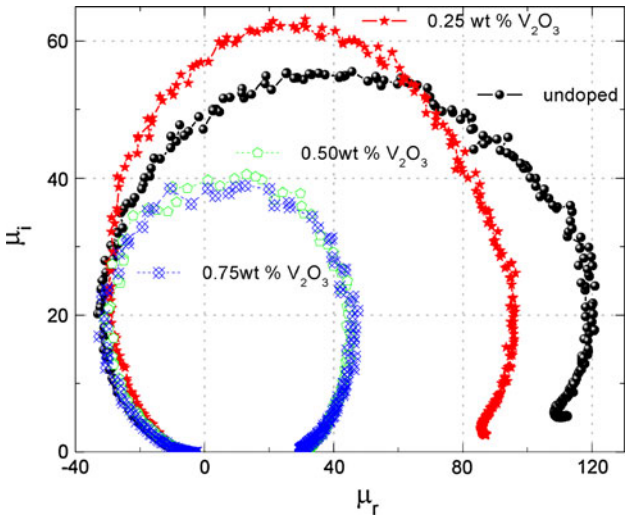

Fig. 5 Comparison between Cole–Cole plots for $Ni_{0.7}Z_{0.3}Fe_2O_4$ ferrites with 0, 0.25 wt% (*solid line*) and 0.50 and 0.75 wt% of V_2O_3 (*dash line*)

Figure 5 shows the evolution of Cole–Cole representations for Ni–Zn ferrites. The samples with lower V_2O_3 concentrations showed a mixed relaxation–resonance dispersion. In fact, this behavior is much closer to a relaxation process, characterized by a decrease in real permeability, μ'; a maximum in imaginary permeability, μ''; and a semicircle in the Cole–Cole representation. In contrast, a natural resonance process was observed in samples with higher V_2O_3 concentration, which exhibit a strong increase in the real part just before the resonance frequency, followed by a vertical decrease through the frequency axis toward negative values, and finally, an asymptotic approximation to zero. The imaginary part shows a strong maximum, and the Cole–Cole plot is a full circle. In a recent article, Herrera [42] makes a comparison between the evaluations of complex permeability on those Ni–Zn ferrites with the use of a resonant equivalent circuit. The experimental results are in agreement with theoretical approximations.

The presence of a wall resonance in the complex permeability analysis is significantly enhanced by the increase in the V doping [41, 42]. The doping of V_2O_3 can significantly improve the dynamic properties Ni–Zn ferrite at the microwave-frequency range.

Magnetization

The room-temperature magnetic hysteresis loops of $Ni_{0.7}Zn_{0.3}Fe_2O_4$ powders doped with Vanadium at different concentrations are given in Fig. 6. The powders were ball milled for 2 h in an agate mortar. Samples with almost the same size and weight were used for these measurements. Table 5 shows the saturation magnetization, M_s, remanent magnetization, M_r, and coercivity, H_c. These parameters were deduced from the magnetization curve for sintered samples. It can be observed that the saturation magnetization, M_s, decreases gradually as the V_2O_3 concentration increases. M_s results are in agreement with a previous study published by Jain et al. [33]. Those authors indicated that the gradual decrease of M_s is the reflection of the effect of the V content on the microstructure of the material similarly to what we have observed for μ_i.

The decrease of saturation magnetization can be explained by the cation distribution between the A and B sites in the ferrite structure. The occupancy of A sites by Fe^{2+} ions displaces some Fe^{3+} ions from A to B sites. This has a direct effect on the increase of the B interaction and

Table 5 Permeability–temperature—(μ–T_C)—evolution

V_2O_3 concentration (wt%)	μ–T_C (K)	μ_i	f_r (MHz)	f_s (MHz)	$4\pi M_s$ (kG)	$4\pi M_r$ (kG)	H_c (Oe)
0	130–553	112.4 (9)	36.6 (5)	44.8 (2)	3.7 (6)	3.0 (2)	4110 (2)
0.25	115–553	87.1 (2)	41.1 (5)	50.7 (4)	3.6 (7)	3.1 (3)	4970 (3)
0.50	38–553	32.2 (2)	73.3 (6)	76.5 (4)	3.5 (7)	2.9 (2)	3279 (3)
0.75	36–553	29.8 (6)	83.9 (3)	86.5 (9)	3.5 (7)	2.9 (2)	4719 (2)

μ_i initial permeability; f_r relaxation frequency; f_s resonance frequency; M_s saturation magnetization; M_r remanence magnetization; and H_c coercitive field

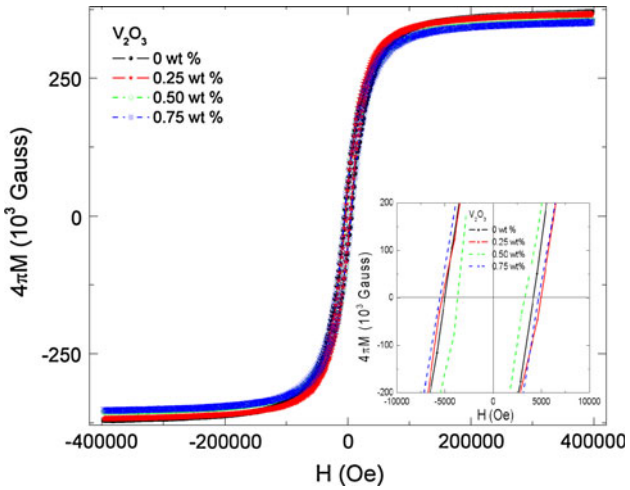

Fig. 6 Comparison between room-temperature M–H graphs of $Ni_{0.7}Zn_{0.3}Fe_2O_4$ with 0, 0.25 wt% (*solid line*); and 0.50 and 0.75 wt% of V_2O_3 (*dash line*). The *inset* is to magnify the coercivity region

the decrease of the A–B interaction, resulting in a reduction of canting within the A lattice. As a consequence, the measured saturation magnetization decreases gradually. On the other hand, Hc increases for doping of 0.25 wt%, and significantly decreases for doping of 0.50 wt%, and increases again for 0.75 wt%. The reduction of grain size by the presence of intergrain porosity is a well-known method to subdivide the ferrite into single-domain particles, which increases the coercivity H_c. This argument is in agreement with the fact that, addition of nonmagnetic V^{3+} enhances the magnetocrystalline anisotropy (K), and given that coercivity is proportional to magnetocrystalline anisotropy ($H_c \propto K$), then, the coercivity increases with the increase of the concentration of V_2O_3.

Conclusions

The observations from XRD, SEM, and magnetic studies are summarized as follows:

1. Single cubic spinel phase of $Ni_{0.7}Zn_{0.3}Fe_2O_4$ stoichiometry was determined by XRD.
2. The lattice parameter increased upon increasing the V^{3+} ion substitution in the $Ni_{0.7}Zn_{0.3}Fe_2O_4$.
3. SEM results and SEM/EDX confirmed that the heat treatment (1250 °C for 24 h) and the location of V_2O_3 lead to abnormal grain growth with intragrain and intergrain porosity (decrease in the magnetic properties).
4. The evolution of morphology shows at higher concentration of Vanadium a compact grain-size distribution. In comparison, lower concentrations of Vanadium result in a wide grain-size distribution.
5. A homogeneous chemical distribution was observed using the permeability thermal spectra.
6. Cole–Cole representations showed a closer relaxation process of the magnetic domain wall for samples with lower concentration. In contrast, a natural resonance process was observed in samples with higher V_2O_3 concentration.
7. The decrease in μ_i was attributed to the abnormal grain growth and the presence of porosity.
8. The use of V_2O_3 and its increasing concentration as a dopant in Ni–Zn ferrites increase the frequency operation and coercivity, H_c, without abruptly degrading the saturation magnetization, M_s.
9. M_s of the Ni–Zn ferrite powders decreased continuously with an increase in Vanadium concentration because of the influence of cationic stoichiometry and their occupancy in the specific sites.
10. The use of Vanadium as a strong dopant for the preparation of the ferrites for any particular application at high frequency proved to be appropriate. This result suggests that ferrites treated in the manner presented in this article, could be good candidates as radar-absorbing materials, presenting a broad response at the microwave-frequency range

Acknowledgements The authors thank CONACyT for the student fellowships, Grant No. 170588, 129569, and PAPPIT No. IN116903. The authors would like to thank especially to MSc. Leticia Baños, MSc Adriana Tejeda-Cruz, Dr. José Guzmán, and Dr. Gabriel Lara for their assistance in XRD and SEM characterization; and the Instituto de Investigaciones en Materiales-UNAM for the facilities to achieve this research, and the Instituto de Ciencias Nucleares-UNAM.

References

1. Valenzuela R (1994) Magnetic ceramics. Cambridge University Press, Cambridge
2. Chen CW (1977) Magnetism and metallurgy of soft magnetic materials. North Holland, Amsterdam
3. Nakamura T (1997) J Magn Magn Mater 168:285
4. Zhang L, Liu X, Guo X, Su M, Xu T, Song X (2010) Chem Eng J. doi:10.1016/j.cej.2011.08.041
5. Lima UR, Nasar MC, Nasar RS, Rezende MC, Araújo V (2008) J Magn Magn Mater 320:1666
6. Buswell M (1989) Microwave Theory Tech 37:860
7. Srinivasan TT, Ravindranathan P, Cross LE, Roy R, Newnham RE, Sankar SG, Patil KC (1988) J Appl Phys 63:3789
8. Kavas H, Baykal A, Toprak MS, Köseoğlu Y, Sertkol M, Aktas B (2009) J Alloys Compds 479:49
9. Sertkol M, Köseoğlu Y, Baykal A, Kavas H, Toprak MS (2010) J Magn Magn Mater 322:866
10. Atkher Hossain AKM, Mahmud ST, Seki M, Kawai T, Tabata H (2007) J Magn Magn Mater 312:210
11. Sertkol M, Köseoğlu Y, Baykal A, Kavas H, Bozkurt A, Toprak MS (2009) J Alloys Compds 486:325
12. Drofenik M, Žnidaršič A, Makovec D (1998) J Am Ceram Soc 81(11):2841

13. Chen SH, Chang SC, Tsay CY, Liu KS, Lin IN (2001) J Eur Ceram Soc 21:1931
14. Janghorban AK, Shokrollahi H (2007) J Magn Magn Mater 308:238
15. Rodriguez-Carvajal J (1990) FULLPROF: a program for rietveld refinement and pattern matching analysis abstracts of the satellite meeting on powder diffraction of the XV congress of the IUCr, Toulouse, France, p 127
16. Rodriguez-Carvajal J, Roisnel T (1998) Newsletter 20:35
17. Cedillo E, Ocampo J, Rivera V, Valenzuela R (1980) J Phys E Sci Instrum 13:383
18. Kasapoğlu N, Baykal A, Toprak MS, Koseoğlu Y, Bayrakdar H (2007) Turk J Chem 31:659
19. Baykal A, Kasapoğlu N, Koseoğlu Y, Toprak MS, Bayrakdar H (2008) J Alloys Compds 464:514
20. Akther S, Choudhury MDA, Rahman J (2009) J Bangladesh Acad Sci 33(2):145
21. Hsu J-Y, Ko W-S, Chen C-J (1995) IEEE Trans Magn 31(6):3994
22. Jean J-H, Lee C-H (2001) Jpn J Appl Phys 40:2232
23. Hu J, Yan M, Luo W (2005) Phys B 368:251
24. Shokrollahi H (2008) J Magn Magn Mater 320:463
25. Herrera G, Rosales Escárcega IEA, Montiel H, Valenzuela R (2004) Study of the resonance-relaxation phenomena of Ni–Zn ferrites doped with V_2O_3 by high-frequency impedance spectroscopy, vol 1. Magnetic Materials, Singapore, Works Scientific eProceedings of PFAM XII, p 377
26. Arcos D, Vázquez M, Valenzuela R, Vallet-Regí M (1999) J Mater Res 14(3):861
27. Narayan R, Tripathi RB, Das BK, Jain GC (1983) J Mater Sci 18(6):1583. doi:10.1007/BF00542050
28. Mirzaee O, Golozar MA, Shafyei A (2008) Mater Charact 59:638
29. Mirzaee O, Shafyei A, Golozar MA, Shokrollahi H (2008) J Alloys Compds 461:312
30. Sun J, Li J, Sun G (2002) J Magn Magn Mater 250:20
31. Shichijo Y, Tsuya N, Suzuki K (1961) J Appl Phys 32(3):386s
32. Lebourgeois R, Duguey S, Ganne J-P, Heintz J-M (2007) J Magn Magn Mater 312:328
33. Jain GC, Das BK, Tripathi RB, Narayan Ram (1982) IEEE Trans Magn 18(2):776
34. Rasband W (2010) ImageJ version 1.43u. National Institute of Health, USA
35. Jankovskis J (2002) In: Scientific proceedings of RTU series 7, telecommunications and electronics, vol 2. Institute of Radioelectronics, Riga, Latvia, pp 68–77
36. Azadmanjiri J (2008) Mater Chem Phys 109:109
37. Rao BP, Rao KH, Sankaranarayana G, Paduraru A, Caltun OF (2005) J Optoelectron Adv Mater 7(2):697
38. Chikazumi S (1977) Physics of ferromagnetism. Clarendon Press, Oxford
39. Herrera M, Montiel H, Valenzuela R (2005) In: Proceedings of the 9th international conference on ferrites ICF9, 2004 edn, San Francisco, USA, August
40. Herrera G (2005) Master′s Thesis, Instituto de Investigaciones en Materiales, UNAM
41. Rao BP, Kim C-O, Kim C-G, Caltun OF (2007) J Optoelectron Adv Mater 9(4):1151
42. Herrera G (2010) J Appl Phys 108:103901
43. Snoek JL (1948) Physica 14(4):207